



# An efficiency calibration method of segmented gamma scanning in reconstructing radioactive waste drum activity

Honglong Zheng<sup>1</sup> · Xianguo Tuo<sup>1</sup> · Zhou Wang<sup>1</sup> · Rui Gou<sup>1</sup> · Qi Liu<sup>1</sup> · Qiang Li<sup>1</sup> · Rui Shi<sup>1</sup> · Guang Yang<sup>2</sup>

Received: 16 August 2023 / Revised: 10 October 2023 / Accepted: 28 November 2023 / Published online: 23 January 2024  
© The Korean Physical Society 2024

## Abstract

For measuring radioactive waste drum, the segmented gamma scanning (SGS) is a quick and effective procedure. The accuracy of reconstructed radioactivity in the drum is directly impacted by SGS efficiency matrix. To overcome the challenges of restricted experimental source and excessive workload in existing SGS efficiency calibration methods, a new SGS efficiency calibration method is presented. The point source efficiency function calculates the non-attenuation efficiency of each voxel in the calibrated segment. The voxel attenuation efficiency is corrected by the linear attenuation coefficient for segments' absorption. The attenuation efficiency for the segment is calculated as the weighted average of all voxel attenuation efficiencies in a segment. The waste drum sample is filled with a random mixture of 0.33 g·cm<sup>-3</sup> aluminium silicate fibre, 0.64 g·cm<sup>-3</sup> wood fibre, 1.84 g·cm<sup>-3</sup> polyvinyl chloride plastic and a point source <sup>60</sup>Co of 1.244 × 10<sup>5</sup> Bq. The SGS system and the waste drum sample are used to complete SGS experimental measurement, efficiency calibration and activity reconstruction. Result shows that the relative deviations of reconstructed activity are – 15.39–30.98% for the extreme case where just a point source <sup>60</sup>Co is placed at 16 positions in the drum with different heights and eccentric distances. This relative deviation rang of reconstructed activity meets the needs of most users. Compared with other methods which have complicated computational processes, the main benefit of this work is to present a low-performance and easy-to-implement additional alternative to commercial software or existing approaches.

**Keywords** Radioactive waste drum · Efficiency calibration · Segmented gamma scanning · MLEM algorithm · Reconstructed activity

## 1 Introduction

The material, the radioisotope and the radioactivity of the waste drum are important for discrimination and categorization of radioactive waste drum in the waste disposal. According to the national standard, it is necessary to measure the gamma radiation of the radioactive waste drum. Because of its nondestructive, fast and low-cost benefits, segmented gamma scanning (SGS) has been frequently employed to assay the radioactive waste drum [1–3]. SGS technique decreases transverse heterogeneity by spinning the waste drum at a constant speed, allowing the basic assumption that

homogeneous distribution of materials and radioisotopes in the segment to be met [4]. It uses longitudinal segmentation to represent vertical heterogeneity distribution of waste drum. The waste drum is measured by SGS system to identify radioisotope and calculate radioactivity.

The efficiency calibration is an important work in SGS measurement, which directly impacts the accuracy of reconstructed activity. Because of the diversity of materials and radioisotopes in the drum, it is difficult to complete the efficiency calibration experimentally [5, 6]. The shell-source calibration method is an equivalent calibration method [7, 8], in which multiple experiential line sources with the same activity are evenly placed in the drum to simulate the uniform distribution of radioactivity. When the radioactive level and the content of each segments are different, the shell-source calibration method is also limited. Monte Carlo simulation is a feasible method in theory, but it is limited to a great amount of calculation and long-time simulation

✉ Honglong Zheng  
zhenghswust@126.com

<sup>1</sup> Sichuan University of Science & Engineering,  
Zigong 643000, China

<sup>2</sup> Chengdu University of Technology, Chengdu 610059, China

[9, 10]. Those methods have better computational accuracy, whilst have complicated computational processes [2, 11].

The point source efficiency function can calculate the point source efficiency of different gamma energy at different positions in three-dimensional space and it has been successfully applied to the volume source passive efficiency calibration [12, 13]. During SGS measurement, the gamma ray emitted from the segment is absorbed not only by the current segment, but also by the adjacent segment before entering the detector. The non-attenuation efficiency of every voxel in the segment is calculated by the point source efficiency function. The voxel attenuation efficiency is corrected by the linear attenuation coefficient for segments' absorption. The attenuation efficiency for the segment is calculated as the weighted average of all voxel attenuation efficiencies in a segment. In this work, a new SGS efficiency calibration method based on the point source efficiency function is proposed. The accuracy and the effectiveness of this method are evaluated by experimental measurement and analysis. Compared with existing SGS efficiency calibration methods limited experimental source, large workload and complicated computational processes, this method improves the convenience of SGS efficiency calibration.

## 2 Methods

### 2.1 Activity reconstruction equation

In SGS measurement, materials and gamma isotopes in the segment of drum are homogeneously distributed by spinning the drum at a constant speed. The waste drum is divided into  $N$  segments, the transmission source and the detector are stepped up vertically, and each segment is measured by the detector. SGS measurement includes the transmission measurement and the emission measurement.

(1) Transmission measurement.

The transmission measurement for a waste drum is achieved by the transmission source and the detector. The linear attenuation coefficient of gamma ray in each segment is calculated by Eq. (1).

$$\mu_j(E) = -\frac{1}{d} \ln\left[\frac{N_j(E)}{N_0(E)}\right] \tag{1}$$

where  $E$  is the energy of gamma ray,  $N_0(E)$  is the intensity of initial gamma ray,  $N_j(E)$  is the intensity of gamma ray that transmitted through the  $j$ 'th segment ( $1 \leq j \leq N$ ),  $\mu_j(E)$  is the linear attenuation coefficient of gamma ray in the  $j$ 'th segment,  $d$  is the diameter of the waste drum. In the  $j$ 'th segment, the relationship between  $\mu_j(E)$  and  $E$  is shown in Eq. (2).

$$\mu_j(E) = a_0 + a_1 \exp(-E/a_2) + a_3 \exp(-E/a_4) \tag{2}$$

where  $a_i(i=0,1,\dots,4)$  are parameters.

(2) Emission measurement.

The emission measurement for a waste drum is achieved by only the detector. The activity reconstruction equation for SGS measurement is shown in Eq. (3).

$$\begin{bmatrix} \epsilon_{11}(E) & \epsilon_{12}(E) & \dots & \epsilon_{1j}(E) & \dots & \epsilon_{1N}(E) \\ \epsilon_{21}(E) & \epsilon_{22}(E) & \dots & \epsilon_{2j}(E) & \dots & \epsilon_{2N}(E) \\ \vdots & \vdots & \vdots & \vdots & \vdots & \vdots \\ \epsilon_{i1}(E) & \epsilon_{i2}(E) & \dots & \epsilon_{ij}(E) & \dots & \epsilon_{iN}(E) \\ \vdots & \vdots & \vdots & \vdots & \vdots & \vdots \\ \epsilon_{N1}(E) & \epsilon_{N2}(E) & \dots & \epsilon_{Nj}(E) & \dots & \epsilon_{NN}(E) \end{bmatrix} \begin{bmatrix} A_1(E) \\ A_2(E) \\ \vdots \\ A_j(E) \\ \vdots \\ A_N(E) \end{bmatrix} = \begin{bmatrix} p_1(E) \\ p_2(E) \\ \vdots \\ p_i(E) \\ \vdots \\ p_N(E) \end{bmatrix} \tag{3}$$

where  $\epsilon_{ij}(E)$  is the detection efficiency of the detector at the  $i$ 'th position for the  $j$ 'th segment ( $1 \leq i \leq N, 1 \leq j \leq N$ ),  $A_j(E)$  is the activity of the  $j$ 'th segment,  $p_i(E)$  is the projection at the  $i$ 'th position,  $p_i(E) = n_i(E)/[f(E)t]$ ,  $n_i(E)$  is the net area of full-energy peak,  $f(E)$  is the branching ratio at  $E$ ,  $t$  is the measurement time of one segment.

### 2.2 Efficiency calculation method

The detection efficiency  $\epsilon_{ij}(E)$  is an important element for accurately establishing activity reconstruction equation from Eq. (3). A new SGS efficiency calibration method is presented in this work and it includes four steps: (1) calculate the linear attenuation coefficient by the transmission measurement; (2) calculate the non-attenuation efficiency of every voxel by the point source efficiency function; (3) calculate the linear attenuation length of gamma ray in the segment; (4) calculate the attenuation efficiency with the linear attenuation coefficient, the non-attenuation efficiency of voxel and the linear attenuation length. Efficiency calculation steps in reconstructing activity of the drum are shown in Fig. 1.

(1) Point source efficiency function.

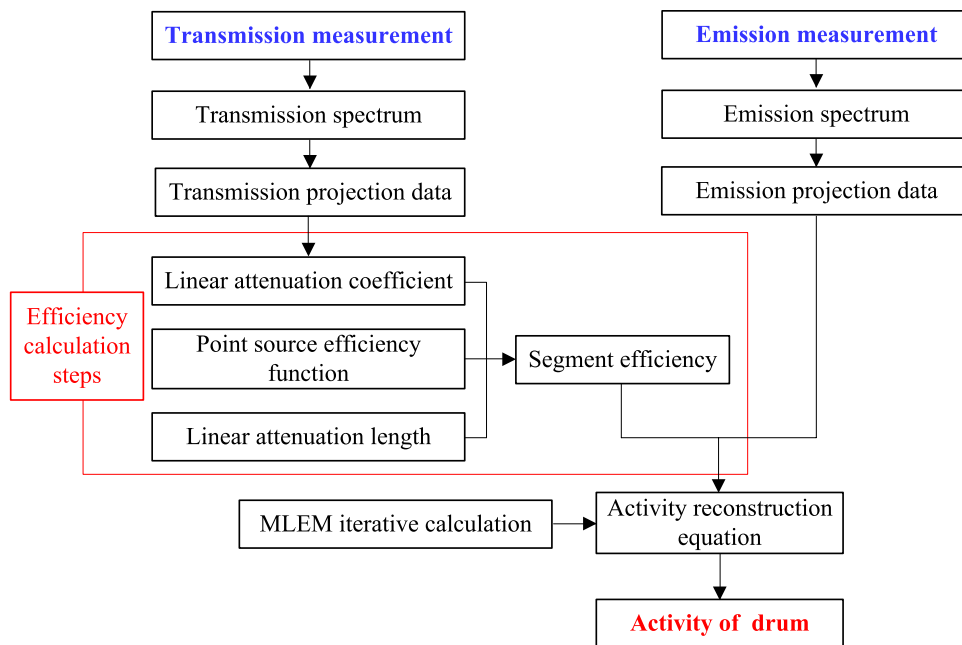
The gamma point source is placed in the detection space in front of SGS system. Detection efficiencies of multiple evenly spaced points in this space are experimentally measured. The position of the point source is  $(x, y, z)$ . According to detection efficiencies of different spatial locations and different gamma energies, the point source efficiency function model (Eq. 4) is adopted to determined parameters by fitting [14].

$$\epsilon(x, y, z, E, b_i) = \frac{e^{-b_1(b_2x^2+b_3z^2)}e^{-b_4y+b_5 \ln(E)+b_6}}{b_7 + b_8y + b_9y^2} \tag{4}$$

where  $\epsilon(x, y, z, E, b_i)$  is the point source efficiency,  $b_i$  ( $i = 1, 2, \dots, 9$ ) are parameters of function.

(2) Linear attenuation length of gamma ray in the segment.

**Fig.1** Activity reconstruction of the drum



A drum is divided into  $N$  segments and each segment is divided into  $K$  voxels. Before being measured by the detector, gamma rays emitted from the voxel are inevitably attenuated by one or more segments. In each segment, the attenuation length of gamma rays emitted by the  $k$ 'th voxel is  $T_{kj}$  ( $1 \leq k \leq K$ ) and the calculation model is shown in Fig. 2.

When the  $i$ 'th segment is measuring by the detector, the  $k$ 'th voxel (point G) in the  $j$ 'th segment is projected onto the  $i$ 'th segment (point B) in Fig. 2a. Point A is the centre of the fronting surface of the detector.  $L_1$  is the distance between point B and point A. Point  $O_2$  is the centre of the  $i$ 'th segment.  $L_2$  is the distance between point  $O_2$  and point A.  $\theta$  is the angle between  $L_1$  and  $L_2$ .  $L_1$  is divided into  $L_3$  (outside line section AD) and  $L_4$  (inside line section BD) by the drum wall.  $R$  is the radius of the drum.  $L_5$  is the distance between point A and point G.  $\varphi$  is the angle between  $L_1$  and  $L_5$ .  $L_6$  is the distance between point G and point E and is the total attenuation length of gamma ray in the drum. The coordinates of points A, B, C, G, and  $O_2$  are

$(0, y_H, 0)$ ,  $(x, y, 0)$ ,  $(0, y, 0)$ ,  $(x, y, z)$ , and  $(0, y_0, 0)$ , respectively, with  $O_1$  as the coordinate origin. The lengths of  $L_1$ – $L_6$ , as well as the values of the angle  $\theta$  and  $\varphi$ , can be computed using the trigonometric relationship.

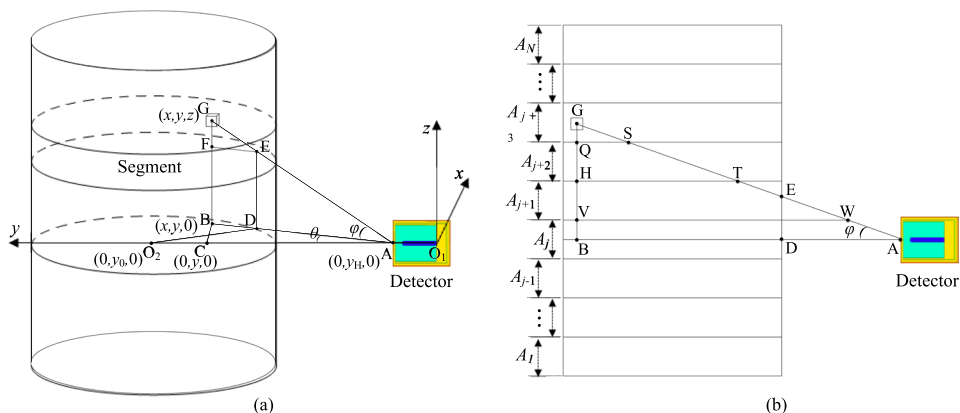
When the detector detects the  $j$ 'th segment at the  $i$ 'th segment height, the attenuation length of the  $k$ 'th voxel emitting gamma rays in the  $j$ 'th segment can be determined in each segment using the voxel coordinates  $(x, y, z)$ , the total length of gamma rays attenuation in the drum ( $L_6$ , line segment GE), the angle  $\varphi$  and the individual segment height  $h$  in Fig. 2b.

When  $j = i$ , the voxel emitting gamma rays are only attenuated in the current segment. The attenuation length is calculated as

$$T_{kj} = L_6 \tag{5}$$

When  $j > i$ , the voxel emitting gamma rays are attenuated in multiple segments. Starting from the  $j$ 'th segment where

**Fig.2** The calculation model of attenuation length



the  $k$ 'th voxel is located, the attenuation lengths in the segments are orderly calculated as

$$T_{kj} = \frac{z - (j - i) \cdot h + 0.5 \cdot h}{\sin \varphi} \tag{6}$$

$$T_{k[j-1]} = \frac{z - (j - 1 - i) \cdot h + 0.5 \cdot h}{\sin \varphi} - T_{kj} \tag{7}$$

$$T_{k[j-2]} = \frac{z - (j - 2 - i) \cdot h + 0.5 \cdot h}{\sin \varphi} - T_{k[j-1]} - T_{kj} \tag{8}$$

Until the gamma rays transmit through the waste drum, the attenuation length in the last segment is calculated as

$$T_{kj'} = L_6 - \sum_{l=j'+1}^j T_{kl} \tag{9}$$

When  $j < i$ , the voxel emitting gamma rays are attenuated in multiple segments. Starting from the  $j$ 'th segment where the  $k$ 'th voxel is located, the attenuation lengths in the segments are orderly calculated as

$$T_{kj} = \frac{|z| - (i - j) \cdot h + 0.5 \cdot h}{\sin \varphi} \tag{10}$$

$$T_{k[j+1]} = \frac{|z| - [i - (j + 1)] \cdot h + 0.5 \cdot h}{\sin \varphi} - T_{kj} \tag{11}$$

$$T_{k[j+2]} = \frac{|z| - [i - (j + 2)] \cdot h + 0.5 \cdot h}{\sin \varphi} - T_{k[j+1]} - T_{kj} \tag{12}$$

Until the gamma rays transmit through the waste drum, the attenuation length in the last segment is calculated as

$$T_{kj'} = L_6 - \sum_{l=j}^{j'-1} T_{kl} \tag{13}$$

(3) Segment efficiency calculation.

The non-attenuation efficiency of every voxel in the segment is calculated by Eq. (4) that is  $\varepsilon_{ijk}(E) = \varepsilon(x, y, z, E, b_i)$ . The voxel attenuation efficiency is corrected by the linear attenuation coefficient for segments' absorption. The attenuation efficiency for the segment is calculated as the weighted average of all voxel attenuation efficiencies in this segment. The detection efficiency of detector to the  $j$ 'th segment at the  $i$ 'th detection position is calculated as

$$\varepsilon_{ij}(E) = \frac{1}{K} \sum_{k=1}^K \varepsilon_{ijk}(E) \exp\left\{-\sum_{j=1}^N [\mu_j(E)T_{kj}]\right\} \tag{14}$$

where  $\varepsilon_{ijk}(E)$  is the non-attenuation efficiency of the  $k$ 'th voxel in the  $j$ 'th segment at the  $i$ 'th detection position,  $\mu_j(E)$  is the linear attenuation coefficient of gamma energy  $E$  in the  $j$ 'th segment,  $T_{kj}$  is the linear attenuation length of gamma ray in the  $j$ 'th segment.

**2.3 Iterative calculation**

Amongst various iterative algorithms for reconstructing radioactivity, the maximum likelihood expectation maximisation (MLEM) algorithm is a common choice [15, 16]. Equation (3) is solved by the MLEM algorithm to calculate the radioactivity  $A_j(E)$ . The iterative format of MLEM algorithm is expressed as Eq. (15).

$$A_j^{(k+1)} = \frac{A_j^{(k)}}{\sum_{i=1}^N \varepsilon_{ij}} \sum_{i=1}^N \varepsilon_{ij} \frac{p_i}{\sum_{l=1}^N \varepsilon_{il} A_l^{(k)}} \tag{15}$$

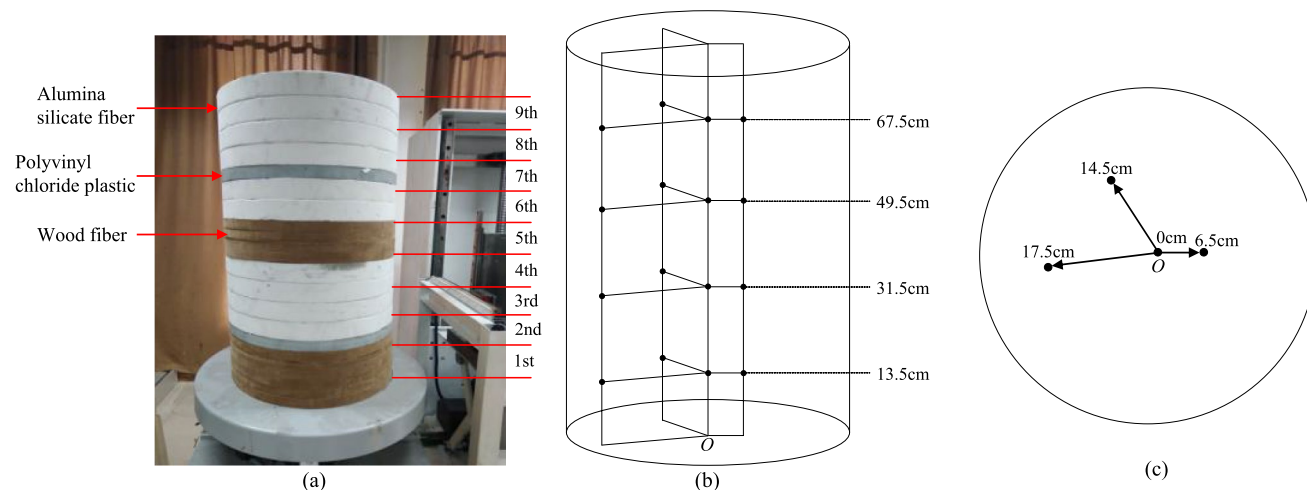
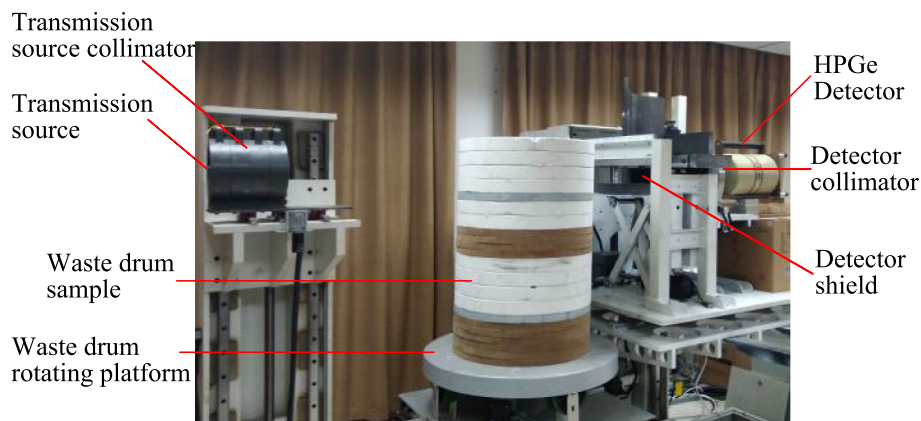
where  $k$  is the number of iteration,  $A_j^{(k+1)}$  and  $A_j^{(k)}$  are the new and current estimates respectively,  $\varepsilon_{ij}$  is the detection efficiency of the detector at the  $i$ 'th position for the  $j$ 'th segment,  $p_i$  is the projection value.

**3 Experiments**

**3.1 SGS system and waste drum sample**

The SGS system mainly consists of the transmission source, the transmission source collimator, the waste drum rotating platform, the HPGe detector, the detector collimator and the detector shield, amongst other components. Figure 3 shows the dimensions of each component. The transmission source is  $^{152}\text{Eu}$ , and it has a  $2.484 \times 10^8$  Bq activity. The HPGe detector's relative detection efficiency for 1.332 MeV is 50% and the energy resolution (FWHM) is 1.9 keV. The transmission source collimator, the detector collimator and the shield are made of lead. The transmission source and detector are always on the same horizontal axis, with a line connecting them running through the waste drum's centre.

Figure 4a shows the waste drum sample, which is filled with a random mixture of alumina silicate fibre (density is  $0.33 \text{ g}\cdot\text{cm}^{-3}$ ), wood fibre (density is  $0.64 \text{ g}\cdot\text{cm}^{-3}$ ) and polyvinyl chloride plastic (density is  $1.84 \text{ g}\cdot\text{cm}^{-3}$ ). The whole waste drum is divided into nine segments during the SGS measurement. Due to a paucity of experimental sources, the radioisotope in the drum for the emission measurement is only a point source  $^{60}\text{Co}$  (activity is  $1.244 \times 10^5$  Bq), which emits gamma rays with energies of 1.173 MeV (99.87%)

**Fig.3** The SGS system**Fig.4** The waste drum sample and the position distribution of the point source  $^{60}\text{Co}$ 

and 1.332 MeV (99.982%). Figure 4b and c show the position distribution of the point source  $^{60}\text{Co}$  in the drum, with heights of 13.5 cm, 31.5 cm, 49.5 cm and 67.5 cm, respectively, and eccentric distances of 0 cm, 6.5 cm, 14.5 cm and 17.5 cm, for a total of 16 positions.

### 3.2 Measurement steps

**Step 1:** Construct the 200 L waste drum sample with the alumina silicate fibre, wood fibre, polyvinyl chloride plastic and a point source  $^{60}\text{Co}$ .

**Step 2:** Put the waste drum on the rotating platform. The transmission source and the detector are set in the detection position of first segment.

**Step 3:** Rotate this platform at a steady speed.

**Step 4:** Turn on the transmission source. The detector obtains a transmission spectrum for the first segment with 120 s.

**Step 5:** Turn off the transmission source. The detector obtains an emission spectrum for the first segment with 180 s.

**Step 6:** Lift the transmission source and the detector up to the detection position of second segment. Repeat step 4 and step 5 to complete the second segment measurement.

**Step 7:** Repeat step 4, step 5 and step 6 until complete nine segments measurement of the waste drum.

**Step 8:** Change the position of the point source in the drum.

**Step 9:** Repeat step 4, step 5, step 6, step 7 and step 8 to complete SGS measurements of the point source at 16 positions in the drum.

**Fig. 5** Measurement steps of the waste drum

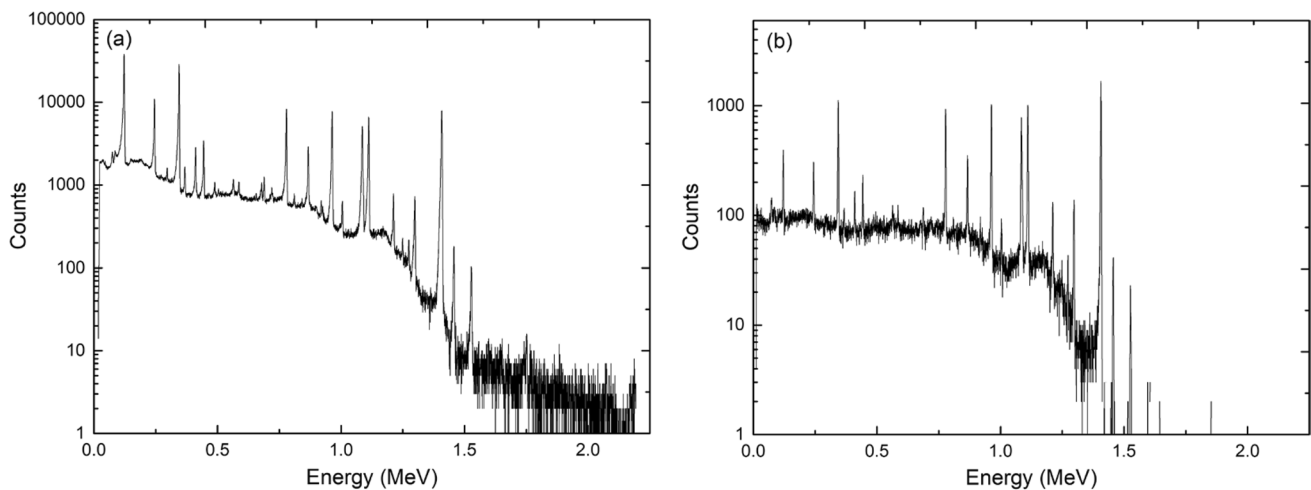
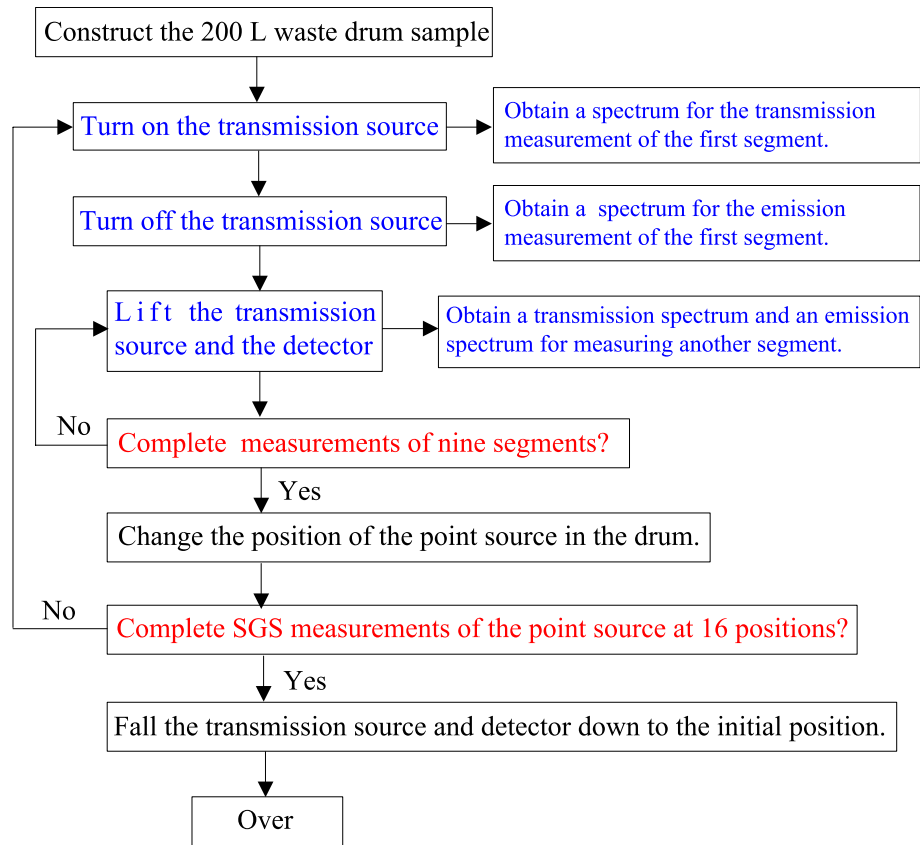


**Fig. 6** The spectrum in transmission measurement

Step 10: Fall the transmission source and detector down to the initial position.

Measurement steps of the waste drum is shown in Fig. 5.

### 3.3 Measurement data

(1) Transmission measurement data.

In transmission measurement, the point source  $^{152}\text{Eu}$  emits main six gamma rays with energies of 0.122 MeV (28%), 0.344 MeV (26.2%), 0.779 MeV (12.7%), 0.964 MeV

**Table 1** Net counts of characteristic peak of six gamma energies in transmission measurement

	0.122 MeV	0.344 MeV	0.779 MeV	0.964 MeV	1.112 MeV	1.408 MeV
No sample	203,904	161,678	47,210	48,495	42,086	55,618
1st	1504	6007	4807	6134	6195	10,623
2nd	1273	4294	3412	4310	4467	7414
3rd	14,302	31,472	15,905	17,983	16,673	25,009
4th	16,324	35,015	17,310	19,294	17,579	26,389
5th	1364	5658	4846	6088	6188	10,193
6th	19,753	39,459	18,611	20,811	19,119	28,133
7th	209	386	169	216	262	569
8th	16,740	34,906	19,328	19,253	18,086	26,562
9th	16,941	35,143	17,348	19,314	18,141	26,847

(14.23%), 1.112 MeV (13.35%) and 1.408 MeV (20.57%). According to measurement steps of the waste drum in Fig. 5, a spectrum before placing the waste drum on the rotating platform is obtained and shown in Fig. 6a, and nine spectrums for measuring nine segments after placing the waste

drum on the rotating platform are obtained by the detector in transmission measurement. As an example, the spectrum for the first segment in transmission measurement is shown in Fig. 6b. Net counts of characteristic peaks corresponding to these six gamma energies are calculated with these

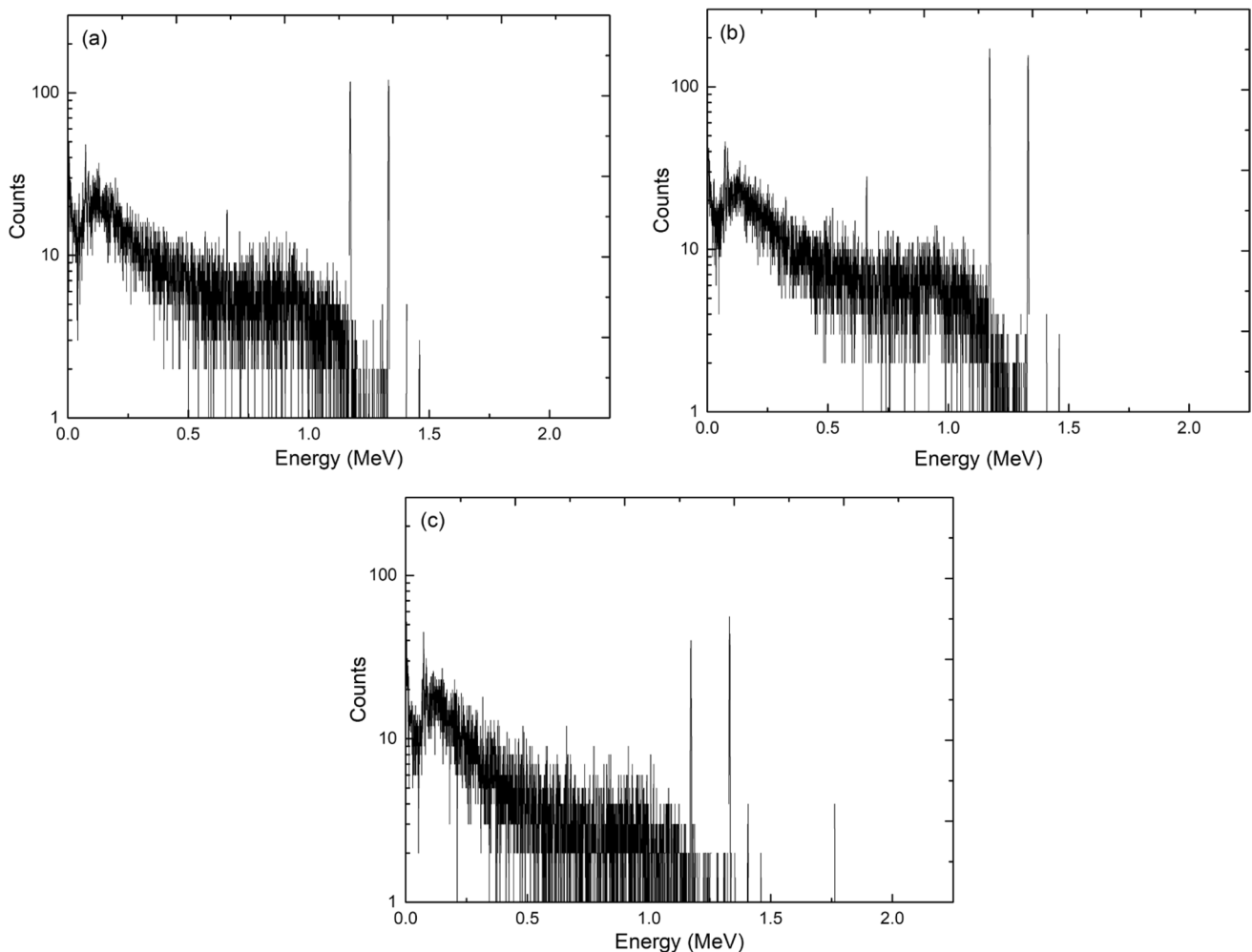


**Fig. 7** The spectrum in emission measurement when the height of  $^{60}\text{Co}$  is 13.5 cm and the eccentric distance of  $^{60}\text{Co}$  is 0 cm in the drum

ten spectrums in transmission measurement and shown in Table 1.

(2) Emission measurement data.

According to this waste drum sample, a point source  $^{60}\text{Co}$  is placed at 16 positions in the drum. For each point source position, nine spectrums for nine segments are obtained by the detector in emission measurement, for a total of 144 spectrums. As an example, when the height of  $^{60}\text{Co}$  is 13.5 cm and the eccentric distance of  $^{60}\text{Co}$  is 0 cm, nine spectrums are measured by the detector, there are two characteristic peaks of 1.173 MeV and 1.332 MeV in the

spectrum measured by the detector for 1st–3rd segments and not characteristic peak in the spectrum measured for 4th–9th segments. Spectrums measured by the detector for 1 s–3rd segments are shown in Fig. 7, where Fig. 7a is the spectrum measured for 1st segment, Fig. 7b is the spectrum measured for 2nd segment, Fig. 7c is the spectrum measured for 3rd segment. Net counts of characteristic peak 1.173 MeV and 1.332 MeV are calculated with these spectrums for each point source position in emission measurement and shown in Tables 2 and 3, where  $h$  is the height of  $^{60}\text{Co}$  and  $r$  is the eccentric distance of  $^{60}\text{Co}$  in the drum.

**Table 2** Net counts of characteristic peak 1.173 MeV in emission measurement

$h$ (cm)	$r$ (cm)	Positions of detector								
		1st	2nd	3rd	4th	5th	6th	7th	8th	9th
13.5	0	727	977	224	0	0	0	0	0	0
13.5	6.5	701	974	216	57	0	0	0	0	0
13.5	14.5	871	1125	381	44	0	0	0	0	0
13.5	17.5	953	1322	557	0	0	0	0	0	0
31.5	0	0	48	1093	1390	1266	196	0	0	0
31.5	6.5	0	72	1236	1417	1197	121	0	0	0
31.5	14.5	0	67	1178	1564	1121	123	0	0	0
31.5	17.5	0	156	1379	1725	1028	97	0	0	0
49.5	0	0	0	0	0	951	1445	1130	142	0
49.5	6.5	0	0	0	0	966	1453	1170	120	0
49.5	14.5	0	0	0	45	1066	1682	1255	175	0
49.5	17.5	0	0	0	49	1043	1763	1214	171	0
67.5	0	0	0	0	0	0	38	1150	1425	1104
67.5	6.5	0	0	0	0	0	59	1105	1480	1207
67.5	14.5	0	0	0	0	0	83	1218	1611	1215
67.5	17.5	0	0	0	0	0	66	1211	1702	1210

**Table 3** Net counts of characteristic peak 1.332 MeV in emission measurement

$h$ (cm)	$r$ (cm)	Positions of detector								
		1st	2nd	3rd	4th	5th	6th	7th	8th	9th
13.5	0	771	881	271	0	0	0	0	0	0
13.5	6.5	651	956	271	49	0	0	0	0	0
13.5	14.5	842	1145	377	0	0	0	0	0	0
13.5	17.5	886	1289	555	0	0	0	0	0	0
31.5	0	0	0	1066	1268	1090	194	0	0	0
31.5	6.5	0	82	1054	1394	1108	131	0	0	0
31.5	14.5	0	76	1164	1459	1058	140	0	0	0
31.5	17.5	0	141	1318	1526	1023	93	0	0	0
49.5	0	0	0	0	50	859	1494	1072	142	0
49.5	6.5	0	0	0	41	923	1519	1149	137	0
49.5	14.5	0	0	0	0	967	1544	1199	147	0
49.5	17.5	0	0	0	36	1043	1608	1139	141	0
67.5	0	0	0	0	0	0	33	1055	1490	1139
67.5	6.5	0	0	0	0	0	45	1053	1464	1167
67.5	14.5	0	0	0	0	0	58	1182	1501	1132
67.5	17.5	0	0	0	0	0	64	1178	1633	1134



**Fig.8** Linear attenuation coefficients of gamma rays in the nine segments

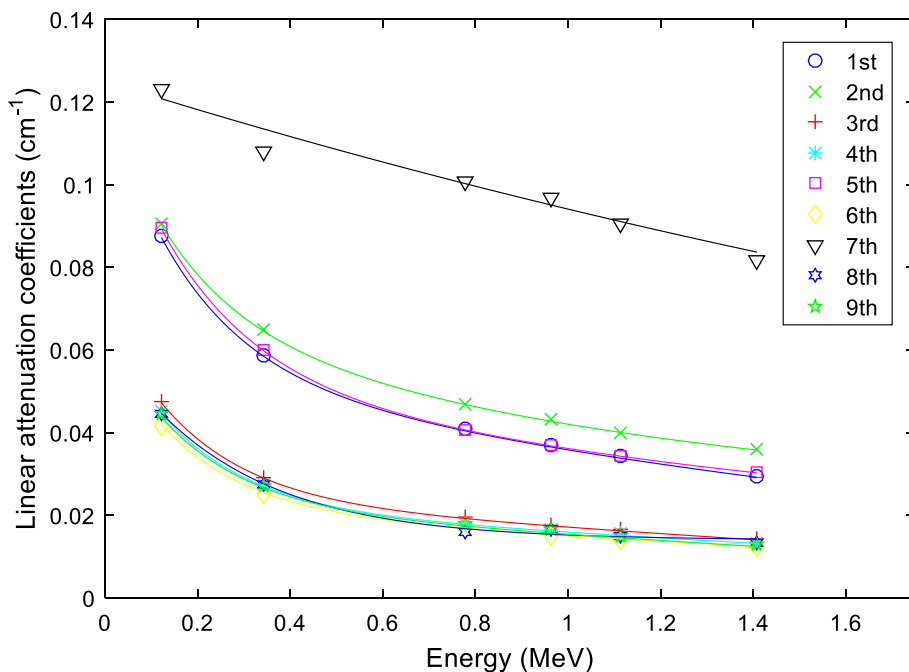


**Table 4** Parameters of function

Segment's number	$a_0$	$a_1$	$a_2$	$a_3$	$a_4$
1st	- 0.009	0.065	2.642	0.066	0.185
2nd	0.021	0.049	1.172	0.051	0.172
3rd	- 149.228	149.252	21,017.706	0.046	0.188
4th	- 163.317	0.045	0.187	163.339	25,929.463
5th	0.009	0.047	1.767	0.067	0.200
6th	- 13.590	0.042	0.185	13.611	2217.468
7th	- 0.006	0.131	3.712	0.000	0.000
8th	0.014	0.024	0.272	0.024	0.272
9th	- 105.197	105.219	15,439.619	0.043	0.189

## 4 Results and discussion

### 4.1 Linear attenuation coefficient of segment

According to these net counts of characteristic peak of six gamma energies in Table 1, Eq. (1) is used to calculate linear attenuation coefficients of different energies in each segment of drum. The linear attenuation coefficients

of 0.122 MeV, 0.344 MeV, 0.779 MeV, 0.964 MeV, 1.112 MeV, and 1.408 MeV in the nine segments of the drum are shown in Fig. 8. Those linear attenuation coefficients in Fig. 8 are fitted with Eq. (2) and the parameters of function are obtained and shown in Table 4.

Gamma energies emitted from the drum are 1.173 MeV and 1.332 MeV, as determined by analysing the spectrum of emission measurement. When these two energies and function parameters in Table 4 are entered into Eq. (2), linear attenuation coefficients of 1.173 MeV and 1.332 MeV in the nine segments are calculated and shown in Table 5.

### 4.2 Efficiency matrix

The centre of the front surface of the HPGe detector is used as the origin to establish the rectangular coordinate system. The spatial area of 60 cm (length) × 60 cm (width) × 50 cm (height) is chosen to arrange the points at a 5 cm interval, and the point sources <sup>137</sup>Cs and <sup>60</sup>Co are placed on the points to measure the experimental efficiency of the point source in the spatial area. Those experimental point source efficiency are fitted using Eq. (4), and parameters of function are obtained as  $b_1 = 1.516$ ,  $b_2 = 0.006$ ,  $b_3 = 0.037$ ,  $b_4 = 0.028$ ,  $b_5 = - 0.374$ ,  $b_6 = - 3.151$ ,  $b_7 = 154.079$ ,  $b_8 = - 3.567$ ,  $b_9 = 0.065$ . The point

**Table 5** Linear attenuation coefficients of 1.173 MeV and 1.332 MeV in nine segments

Energy (MeV)	1st	2nd	3rd	4th	5th	6th	7th	8th	9th
1.173	0.033	0.039	0.016	0.015	0.033	0.014	0.090	0.015	0.014
1.332	0.030	0.037	0.015	0.014	0.031	0.013	0.086	0.014	0.013

**Table 6** The attenuation efficiency matrix of 1.173 MeV

Positions of detector	Positions of segment								
	1st	2nd	3rd	4th	5th	6th	7th	8th	9th
1st	$4.68 \times 10^{-5}$	$2.84 \times 10^{-5}$	$1.22 \times 10^{-5}$	$3.51 \times 10^{-6}$	0	0	0	0	0
2nd	$3.10 \times 10^{-5}$	$4.26 \times 10^{-5}$	$4.18 \times 10^{-5}$	$1.55 \times 10^{-5}$	$2.91 \times 10^{-6}$	0	0	0	0
3rd	$9.52 \times 10^{-6}$	$2.91 \times 10^{-5}$	$6.32 \times 10^{-5}$	$4.43 \times 10^{-5}$	$1.20 \times 10^{-5}$	$2.50 \times 10^{-6}$	0	0	0
4th	$1.77 \times 10^{-6}$	$1.10 \times 10^{-5}$	$4.35 \times 10^{-5}$	$6.46 \times 10^{-5}$	$3.19 \times 10^{-5}$	$1.33 \times 10^{-5}$	$1.72 \times 10^{-6}$	0	0
5th	0	$2.67 \times 10^{-6}$	$1.55 \times 10^{-5}$	$4.30 \times 10^{-5}$	$4.67 \times 10^{-5}$	$4.40 \times 10^{-5}$	$6.34 \times 10^{-6}$	$1.04 \times 10^{-6}$	0
6th	0	0	$3.55 \times 10^{-6}$	$1.31 \times 10^{-5}$	$3.20 \times 10^{-5}$	$6.62 \times 10^{-5}$	$1.54 \times 10^{-5}$	$9.19 \times 10^{-6}$	$3.60 \times 10^{-6}$
7th	0	0	0	$2.46 \times 10^{-6}$	$1.22 \times 10^{-5}$	$4.14 \times 10^{-5}$	$2.36 \times 10^{-5}$	$4.08 \times 10^{-5}$	$1.59 \times 10^{-5}$
8th	0	0	0	0	$2.94 \times 10^{-6}$	$9.31 \times 10^{-6}$	$1.54 \times 10^{-5}$	$6.51 \times 10^{-5}$	$4.46 \times 10^{-5}$
9th	0	0	0	0	0	$1.05 \times 10^{-6}$	$6.28 \times 10^{-6}$	$4.48 \times 10^{-5}$	$6.49 \times 10^{-5}$

**Table 7** The attenuation efficiency matrix of 1.332 MeV

Positions of detector	Positions of segment								
	1st	2nd	3rd	4th	5th	6th	7th	8th	9th
1st	$4.88 \times 10^{-5}$	$2.95 \times 10^{-5}$	$1.27 \times 10^{-5}$	$3.65 \times 10^{-6}$	0	0	0	0	0
2nd	$3.24 \times 10^{-5}$	$4.42 \times 10^{-5}$	$4.28 \times 10^{-5}$	$1.60 \times 10^{-5}$	$3.06 \times 10^{-6}$	0	0	0	0
3rd	$1.00 \times 10^{-5}$	$3.02 \times 10^{-5}$	$6.47 \times 10^{-5}$	$4.53 \times 10^{-5}$	$1.25 \times 10^{-5}$	$2.65 \times 10^{-6}$	0	0	0
4th	$1.91 \times 10^{-6}$	$1.15 \times 10^{-5}$	$4.45 \times 10^{-5}$	$6.59 \times 10^{-5}$	$3.32 \times 10^{-5}$	$1.38 \times 10^{-5}$	$1.82 \times 10^{-6}$	0	0
5th	0	$2.81 \times 10^{-6}$	$1.59 \times 10^{-5}$	$4.40 \times 10^{-5}$	$4.84 \times 10^{-5}$	$4.51 \times 10^{-5}$	$6.67 \times 10^{-6}$	$1.10 \times 10^{-6}$	0
6th	0	0	$3.69 \times 10^{-6}$	$1.36 \times 10^{-5}$	$3.33 \times 10^{-5}$	$6.75 \times 10^{-5}$	$1.60 \times 10^{-5}$	$9.40 \times 10^{-6}$	$3.68 \times 10^{-6}$
7th	0	0	0	$2.61 \times 10^{-6}$	$1.27 \times 10^{-5}$	$4.24 \times 10^{-5}$	$2.45 \times 10^{-5}$	$4.11 \times 10^{-5}$	$1.62 \times 10^{-5}$
8th	0	0	0	0	$3.09 \times 10^{-6}$	$9.63 \times 10^{-6}$	$1.60 \times 10^{-5}$	$6.55 \times 10^{-5}$	$4.56 \times 10^{-5}$
9th	0	0	0	0	0	$1.12 \times 10^{-6}$	$6.56 \times 10^{-6}$	$4.51 \times 10^{-5}$	$6.64 \times 10^{-5}$

source efficiency function of the HPGe detector is established with Eq. (4) and these function parameters.

A segment is divided into 828 voxels and the size of every voxel is  $3 \text{ cm} \times 3 \text{ cm} \times 3 \text{ cm}$ . The point source efficiency  $\varepsilon_{ijk}(E)$  in the centre of voxel is calculated by this point source efficiency function. Equation (14) is used to calculate the attenuation efficiency of a segment by combining the point source efficiency  $\varepsilon_{ijk}(E)$ , the attenuation length  $T_{kj}$ , and the linear attenuation coefficient  $\mu_j(E)$ . Attenuation efficiency matrices of 1.173 MeV and 1.332 MeV are calculated as shown in Tables 6 and 7, respectively.

### 4.3 Reconstructed activity and relative deviation

According to these net counts of characteristic peak 1.173 MeV and 1.332 MeV in Tables 2 and 3, the projection data  $p_i(E)$  of each segment is obtained in emission measurement. The projection data, as well as attenuation efficiency matrices of 1.173 and 1.332 MeV are entered into Eq. (3). The MLEM algorithm is used to solve Eq. (3) and the activity of  $^{60}\text{Co}$  in the drum are reconstructed as shown in Table 8.

The larger the eccentric distance of the  $^{60}\text{Co}$  point source in the segment, the larger the reconstructed activity, as seen

in Table 8. The fundamental reason for this is that when the point source approaches the near surface of detector, the detection distance shortens and the medium attenuation weakens, resulting in an increase in the detector count. The lower the end effect, the more precise the detector's detection of gamma rays, and the more accurate the reconstructed activity are when the point source is placed closer to the centre segment of the drum from the vertical direction. The point source  $^{60}\text{Co}$  is positioned in the drum at 16 distinct heights and eccentric distances, with relative deviations of reconstructed activity ranging from  $-15.39$  to  $30.98\%$ , with the majority of relative deviations being less than  $15\%$ .

The effect of the different heights and eccentric distances on the reconstructed activity of the point source  $^{60}\text{Co}$  in the drum is investigated, and relative deviations of reconstructed activity in Table 8 are presented in Fig. 9. Where Fig. 9a shows the effect of the eccentric distance on the relative deviation of reconstructed activity of 1.173 MeV, Fig. 9b shows the effect of the height on the relative deviation of reconstructed activity of 1.173 MeV, Fig. 9c shows the effect of the eccentric distance on the relative deviation of reconstructed activity of 1.332 MeV, and Fig. 9d shows the effect

**Table 8** Reconstructed activity and relative deviation of  $^{60}\text{Co}$  in the drum

Height (cm)	Eccentric distance (cm)	1.173 MeV		1.332 MeV	
		Reconstructed activity (Bq)	Relative deviation (%)	Reconstructed activity (Bq)	Relative deviation (%)
13.5	0	$1.196 \times 10^5$	- 3.86	$1.135 \times 10^5$	- 8.82
13.5	6.5	$1.155 \times 10^5$	- 7.16	$1.071 \times 10^5$	- 13.93
13.5	14.5	$1.415 \times 10^5$	13.68	$1.352 \times 10^5$	8.63
13.5	17.5	$1.630 \times 10^5$	30.98	$1.492 \times 10^5$	19.86
31.5	0	$1.192 \times 10^5$	- 4.23	$1.053 \times 10^5$	- 15.39
31.5	6.5	$1.207 \times 10^5$	- 3.03	$1.097 \times 10^5$	- 11.86
31.5	14.5	$1.210 \times 10^5$	- 2.79	$1.134 \times 10^5$	- 8.87
31.5	17.5	$1.309 \times 10^5$	5.17	$1.194 \times 10^5$	- 4.10
49.5	0	$1.147 \times 10^5$	- 7.80	$1.103 \times 10^5$	- 11.34
49.5	6.5	$1.160 \times 10^5$	- 6.78	$1.150 \times 10^5$	- 7.62
49.5	14.5	$1.321 \times 10^5$	6.14	$1.177 \times 10^5$	- 5.45
49.5	17.5	$1.326 \times 10^5$	6.57	$1.210 \times 10^5$	- 2.76
67.5	0	$1.310 \times 10^5$	5.23	$1.317 \times 10^5$	5.80
67.5	6.5	$1.382 \times 10^5$	11.01	$1.326 \times 10^5$	6.57
67.5	14.5	$1.453 \times 10^5$	16.78	$1.347 \times 10^5$	8.23
67.5	17.5	$1.474 \times 10^5$	18.45	$1.390 \times 10^5$	11.69

of the height on the relative deviation of reconstructed activity of 1.332 MeV.

The relative deviation of reconstructed activity increases with the rise of the eccentric distance, as seen in Fig. 9a and c. It is primarily due to that as the eccentric distance of the point source in the drum increases, the share of attenuation of the point source decreases at the proximal end of the detector and increases at the distal end during rotational measurement, resulting in a larger net peak area of the spectrum and a larger value of the reconstructed radioactivity, as well as a larger relative deviation. Figure 9b and d show that when the height of the point source in the drum grows, the relative deviation of reconstructed activity reduces at first, then increases. Compared with the reconstructed activity for the bottom and top segments of the waste drum, the intermediate segment is less affected by the end effect and the reconstructed activity is more accurate with less relative deviation.

Previous studies have shown that the relative deviation range are generally - 80 to 300% for the extreme case where the radioisotope is a point source in the drum [17]. In this work, a single point source is randomly placed at different heights and eccentric distances in the drum and the relative deviation of reconstructed activity is less than 31%. This work reduces the relative deviation range to some extent. In general, the drum is dispersed with radioisotopes in numerous areas during the actual radioactive waste drum

SGS measurement, which is closer to the ideal state of uniform distribution of isotopes than this work, so the analysis results could be better. As a result, this method proposed in this work can more easily and conveniently achieve the SGS efficiency calibration and this relative deviation rang of reconstructed activity meets the needs of most users.

## 5 Conclusion

An efficiency calibration method of SGS in reconstructing radioactive waste drum activity is proposed. The non-attenuation efficiency of every voxel in the segment is calculated by the point source efficiency function. The voxel attenuation efficiency is corrected by the linear attenuation coefficient. The attenuation efficiency of segment is calculated as the weighted average of all voxel attenuation efficiencies. Combined with this efficiency calibration method, the experimental results show that the relative deviations of reconstructed activity are - 15.39–30.98% for the extreme case where the radioisotope is a point source in the drum. Compared with other methods which have complicated computational processes, this method proposed in this work can more easily and conveniently achieve the SGS efficiency calibration and this relative deviation rang of reconstructed activity meets the needs of most users. For gamma non-destructive measurement of radioactive waste drum, this method has some reference relevance.

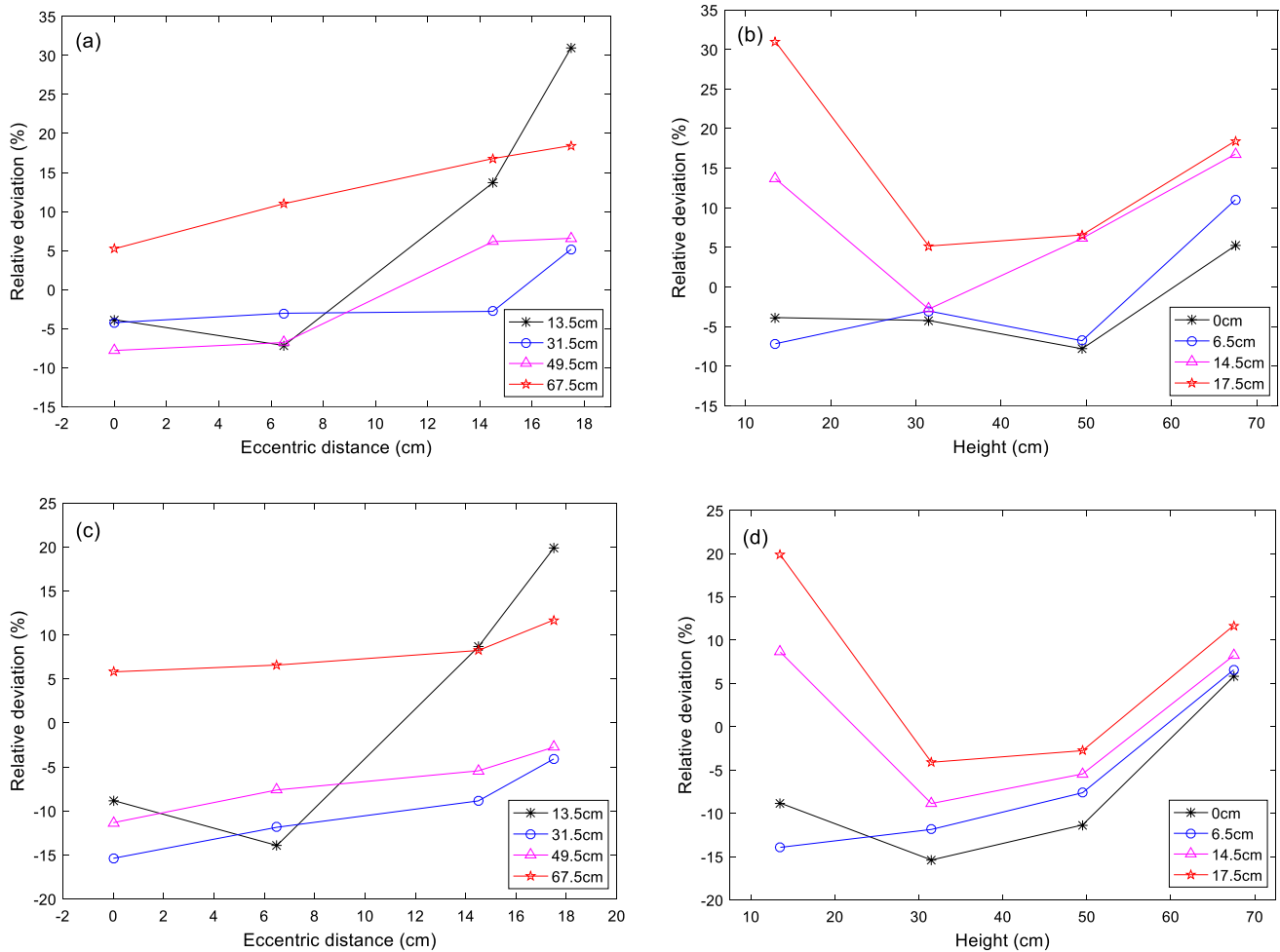


Fig. 9 Effect of height and eccentricity distance on relative deviation

**Acknowledgements** This work is supported by the National Natural Science Foundation of China (No. 42204179, 42374227, 42074218 and 12205210), the Sichuan Science and Technology Program of China (No. 24NSFSC3955 and 2022NSFSC1231) and the Scientific Research and Innovation Team Program of Sichuan University of Science and Engineering (No. SUSE652A001).

## Declarations

**Conflict of interest** Honglong Zheng, Xianguo Tuo and Rui Shi have received research support from National Natural Science Foundation Committee of China. Honglong Zheng and Qi Liu have received research support from Science & Technology Department of Sichuan Province of China. Zhou Wang, Rui Gou, Qiang Li and Guang Yang declare they have no financial interests.

## References

1. T. Bücherl, S. Rummel, O. Kalthoff, Nucl. Instrum. Methods Phys. Res. A **1019**, 165887 (2021)
2. E. Laloy, B. Rogiers, A. Bielen et al., Appl. Radiat. Isot. **175**, 109803 (2021)
3. S.X. Hou, J.J. Luo, R.S. Li et al., Ann. Nucl. Energy. **135**, 106965 (2020)
4. X.F. Mu, R. Shi, G. Luo et al., Appl. Radiat. Isot. **182**, 110123 (2022)
5. M. Toma, O. Sima, C. Olteanu, Nucl. Instrum. Methods Phys. Res. A **580**, 391–395 (2007)
6. T. Boshkova, K. Mitev, Appl. Radiat. Isot. **109**, 114–117 (2016)
7. L.J. Xu, H.S. Ye, W.D. Zhang et al., Nucl. Tech. **38**, 050502 (2015)
8. M. Bruggeman, J. Gerits, R. Carchon, Appl. Radiat. Isot. **51**, 255–259 (1999)
9. S.P. Narayanam, M. Manohari, R. Ramar et al., Appl. Radiat. Isot. **152**, 127–134 (2019)
10. T. Özdemir, Radiat. Phys. Chem. **135**, 11–17 (2017)
11. S. Patra, C. Agarwal, Appl. Radiat. Isot. **153**, 108827 (2019)
12. H. Yücel, S. Zümrüt, R.B. Narttürk et al., Nucl. Eng. Tech. **51**, 526–532 (2019)
13. Z.N. Tian, Y. Zhang, M.Y. Jia et al., Atom. Energy Sci. Tech. **44**, 439–444 (2010)
14. H.L. Zheng, X.G. Tuo, J.Y. Gou et al., Nucl. Elec. Det. Tech. **41**, 24–29 (2021)
15. T. Roy, M.R. More, J. Ratheesh et al., Radiat. Phys. Chem. **130**, 29–34 (2017)

16. K. Wang, Z. Li, W. Feng, Nucl. Instrum. Methods Phys. Res. A **755**, 28–31 (2014)
17. D.Q. Dung, Ann. Nucl. Energy. **24**, 33–47 (1997)

**Publisher's Note** Springer Nature remains neutral with regard to jurisdictional claims in published maps and institutional affiliations.

Springer Nature or its licensor (e.g. a society or other partner) holds exclusive rights to this article under a publishing agreement with the author(s) or other rightsholder(s); author self-archiving of the accepted manuscript version of this article is solely governed by the terms of such publishing agreement and applicable law.